Ocean Engineering 235 (2021) 109331

Contents lists available at ScienceDirect

Ocean Engineering

journal homepage: www.elsevier.com/locate/oceaneng

Propulsion enhancement of flexible plunging foils: Comparing linear theory predictions with high-fidelity CFD results

E. Sanmiguel-Rojas, R. Fernandez-Feria *

Fluid Mechanics Group, Universidad de Málaga, Dr Ortiz Ramos s/n, 29071 Málaga, Spain

ARTICLE INFO

Keywords:
Flexible flapping foil
Propulsion
Fluid–structure interaction

ABSTRACT

The fluid–structure interaction of a flexible plunging hydrofoil immersed in a current is solved numerically to analyze its propulsion enhancement due to flexibility at Reynolds number 10 000. After validating with available experimental data, the code is used to assess analytical predictions from a linear theory. We consider large stiffness ratios, with high thrust enhancement by flexibility, and small mass ratios appropriate for underwater propulsion. The maximum thrust enhancement is observed at the first natural frequency, accurately predicted by the linear theory algebraically. The magnitude of the maximum thrust is over-predicted by the theory as the flapping amplitude increases. For large Strouhal numbers the flow becomes aperiodic, which for large enough amplitudes happens at frequencies below the natural frequency. But even at these Strouhal numbers, the linear theory predicts quite well the frequency of maximum thrust enhancement and optimal propulsive efficiency. We conclude that the linear theory constitutes a reliable and useful guide for the design of underwater flexible flapping-foil thrusters, and we provide a practical chart to easily select the optimal flapping frequency as a function of the actuation point, the stiffness and the mass ratios of the hydrofoil.

1. Introduction

The search for more efficient propellers for small underwater vehicles and more efficient energy harvesting devices based on flapping foils has accelerated in the last few years the interest in the study of the fluid–structure interaction (FSI) of a flexible plate oscillating under water [see, e.g., Anevlavi et al., 2020; Dagenais and Aegerter, 2020; Goza et al., 2020; Manjunathan and Bhardwaj, 2020; Wang et al., 2020; Demirer et al., 2021 for very recent works, and the recent review by Wu et al., 2020]. The enhancement of the propulsive capabilities of passively deformable flapping foils over certain ranges of the structural and kinematic parameters has been analyzed and explained in a large number of works, especially for the simplest configuration of a two-dimensional (2D) flapping foil with chordwise flexibility, both theoretically and numerically for inviscid flows (e.g., Katz and Weihs, 1978; Alben, 2008; Michelin and Llewellyn Smith, 2009; Moore, 2014; Paraz et al., 2016; Floryan and Rowley, 2018), and experimentally and numerically for viscous flows (e.g., Heathcote and Gursul, 2007; Zhu, 2007; Shin et al., 2009; Dewey et al., 2013; Cleaver et al., 2014). In most of these investigations the improvement in the propulsive performance has been related to resonance, i.e. to peaks in the passive deflection amplitude when the forcing frequency of the oscillations is at, or near, the natural frequencies of the fluid–foil system (Alben et al., 2012; Dewey et al., 2013; Quinn et al., 2014; Paraz et al., 2016; Floryan and Rowley, 2018). For relatively small forcing amplitudes, the most relevant of these natural frequencies is the lowest one corresponding to the first mode flapping (Alben, 2008; Moore, 2015). As the amplitude of the oscillations increases, higher modes become more relevant, or even resonance ceases to be the main enhancement mechanism in the propulsive performance of a deformable flapping foil (Ramananarivo et al., 2011; Alben et al., 2012; Quinn et al., 2014; Floryan and Rowley, 2018; Goza et al., 2020).

For very small forcing amplitudes and high Reynolds numbers, one may solve approximately the 2D FSI problem combining the Euler–Bernoulli beam equation with linear potential flow theory for a pitching and plunging foil with the passive flexural deflection approximated by a lower-order polynomial (Fernandez-Feria and Alaminos-Quesada, 2021a). Only the first natural frequency is captured with this approximation, but it is obtained analytically, along with the thrust force and input power, both peaking at, or close to, this natural frequency, and hence the corresponding propulsive efficiency. Although it was shown in Fernandez-Feria and Alaminos-Quesada (2021a) that these analytical results agree quite well with previous ones obtained numerically from a more complete linearized potential flow theory, it remains to investigate to what extent the analytical results can be used to estimate the propulsive performance of actual flexible flapping foils as the flapping

* Correspondence to: Fluid Mechanics Group, Universidad de Málaga, Dr Ortiz Ramos s/n, 29071 Málaga, Spain.
E-mail addresses: enrique.sanmiguel@uma.es (E. Sanmiguel-Rojas), ramon.fernandez@uma.es (R. Fernandez-Feria).

https://doi.org/10.1016/j.oceaneng.2021.109331
Received 8 March 2021; Received in revised form 21 May 2021; Accepted 11 June 2021
Available online 23 June 2021

Nomenclature

$\mathbf{u}$	Nondimensional fluid velocity
η	Propulsive efficiency
ν	Poisson's ratio
ω	Frequency
ψ	Flexural deflection phase shift
ρ	Fluid density
ρ_s	Solid density
$\boldsymbol{\tau}$	Nondimensional stress tensor
ϵ	Foil thickness
a	Nondimensional pivot point location
c	Chord length
C_L	Lift coefficient
C_M	Moment coefficient
S	Thrust coefficient
C_{L_i}	Input lift coefficient
C_{M_i}	Input torque coefficient
C_{P_i}	Input power coefficient
$d(t)$	Nondimensional flexural deflection
d_m	Nondimensional flexural amplitude
d_{TE}	Nondimensional flexural amplitude at the trailing edge
E	Elasticity modulus
f	Frequency in Hz
$h(t)$	Nondimensional plunge motion
h_0	Nondimensional plunge amplitude
I_a	Nondimensional moment of inertia
J_a, J_d, K_d	Structural flexural coefficients
k	Reduced frequency
k_r	Nondimensional natural frequency
k_{r0}	Nondimensional resonant frequency
L_i	Input lift
m	Nondimensional foil mass
M_i	Input torque
p	Nondimensional pressure
R	Mass ratio
Re	Reynolds number
C_T	Thrust coefficient
St	Stiffness ratio
U	Freestream speed
x_0	Nondimensional center of mass
$z_s(x,t)$	Nondimensional foil displacement

amplitude increases, provided that the aspect ratio and the Reynolds number are both large enough. More particularly, it is of great interest to know if the first natural frequency provided by the linear theory from just a simple algebraic equation can be used to predict the actuating frequency for optimal propulsive performance of a flexible plunging foil. This is the problem analyzed in the present work for a 2D flexible plate undergoing a forced plunging motion at the leading edge at Reynolds number 10 000.

2. Formulation of the problem

We consider the fluid–structure interaction of a two-dimensional flexible foil immersed in a current of constant speed U along the $\tilde{x}$-axis of an incompressible fluid and subjected to a prescribed heaving motion $\tilde{h}(t)$ along the axis $\tilde{z}$ perpendicular to the current U and imposed on an arbitrary pivot location $\tilde{a}$ (see sketch in Fig. 1; a tilde ˜ over any symbol means a dimensional quantity whose symbol is used later for its dimensionless counterpart without the tilde). The chord length of the foil at rest is c.

The location of the foil centerline at any instant of time $\tilde{t}$ is $\tilde{z}_s(\tilde{x},\tilde{t})$. If $\tilde{s}$ is the coordinate along it, with $-c/2 \le \tilde{s} \le c/2$, $\rho_s(\tilde{s})$, $\epsilon(\tilde{s})$, and $E(\tilde{s})I(\tilde{s})$ are the hydrofoil density, thickness and flexural rigidity, respectively, where E is Young's elasticity modulus and $I = \epsilon^3/12$ the second moment of area. This quantities are allowed to vary along the foil chord length, so that, for instance, the foil center of mass $\tilde{x}_0$ does not necessarily coincide with its mid-point $\tilde{s} = c/2$ nor with the pivot axis $\tilde{s} = \tilde{a}$. However, most of the numerical results reported below are for a uniform plate with constant density, thickness and rigidity.

We assume a harmonic plunging motion of frequency ω and amplitude $\tilde{h}_0$ of the form $\tilde{h} = \tilde{h}_0 \cos(\omega\tilde{t})$. This motion is produced by a force (per unit length) L_i in the $\tilde{z}$-direction which is computed as a part of the solution of the FSI problem. In addition, a torque M_i (per unit length) has also to be applied at the pivot point to avoid rotation about this point through the FSI, which is also computed as a part of the solution, if needed. It must be noted that, although the location of the (pivot) point where the force L_i is applied to generate the plunging motion is not relevant for a rigid foil, it is for a flexible foil, for the foil bending deflection would depend on the pivot point location and therefore the aerodynamic forces that the fluid exerts on the foil.

From this point on we use dimensionless variables and parameters, most of them designated with the same letter but without the tilde, by scaling all lengths with $c/2$, velocities with U, so that time is scaled with $c/(2U)$, and forces (per unit length) with $\rho U^2 c/2$, where ρ is the fluid density. Thus, the nondimensional plunging motion applied at $s = a$ $(-1 \le a \le 1)$ is

$$h(t) = \mathrm{Re}\left[h_0 e^{ikt}\right], \quad k = \frac{\omega c}{2U}, \tag{1}$$

where k is the standard reduced frequency and Re means real part. Alternatively, one may use the standard Strouhal number

$$St = \frac{2\tilde{h}_0 f}{U} = \frac{h_0 k}{\pi}, \tag{2}$$

where f is the frequency in Hz. In addition to h_0, a and k (or St), other dimensionless parameters characterizing the problem are the mass ratio (R), the stiffness ratio (S) and the Reynolds number (Re), defined as

$$R = \frac{\rho_s \epsilon}{\rho c}, \quad S = \frac{E\epsilon^3}{\rho U^2 c^3} = \frac{12EI}{\rho U^2 c^3}, \quad Re = \frac{\rho U c}{\mu}, \tag{3}$$

respectively, where μ is the fluid viscosity. Note that R and S are in general functions of s. Once the FSI problem is solved as it will be described below, one may compute the force $\mathbf{F}$ that the fluid exerts on the foil's surface, which is decomposed in its thrust and *lift* components. In dimensionless form,

$$C_T(t) = -\frac{F_x}{\frac{1}{2}\rho U^2 c}, \quad C_L(t) = \frac{F_z}{\frac{1}{2}\rho U^2 c}. \tag{4}$$

Likewise, one may compute the nondimensional input force L_i applied at the pivot point to generate the prescribed heaving motion, and, therefore the input power coefficient:

$$C_{L_i}(t) = \frac{L_i}{\frac{1}{2}\rho U^2 c}, \qquad C_{Pi}(t) = C_{L_i}\dot{h}, \tag{5}$$

where a dot means derivative with respect to the (nondimensional) time. In the numerical simulations, only the input power needed to overcome the fluid force on the foil, i.e., $C_{Pi}^F = -C_L\dot{h}$, is computed, which coincides with C_{Pi} for negligible inertia of the foil ($R \to 0$). However, both input powers are obtained from the linear theory analytically.

Since the foil motion is periodic, one is also interested in time-averaged quantities over a (nondimensional) period $T = 2\pi/k$, which are denoted with an over-bar; e.g.,

$$\overline{C}_T = \int_t^{t+2\pi/k} C_T(t)dt, \tag{6}$$

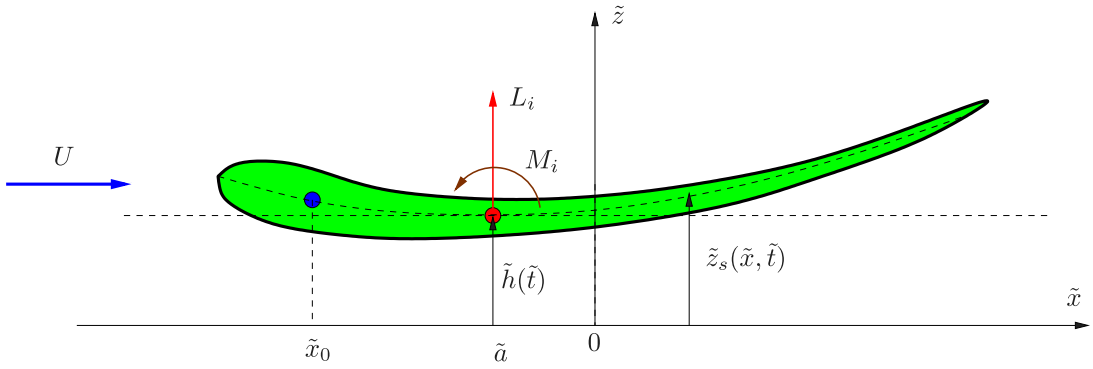

Fig. 1. Schematic of the problem (dimensional quantities).

and similarly for $\overline{C}_L$, $\overline{C}_{L_i}$ and $\overline{C}_{Pi}$. The propulsive (Froude) efficiency is defined as

$$\eta = \frac{\overline{C}_T}{\overline{C}_{Pi}} \,. \tag{7}$$

3. Numerical method

The structural Finite Element Analysis (FEA) was performed with the CFD software Fluent inside the Ansys v20.2 package for multi-physics applications. Specifically, the FSI is performed by solving simultaneously the flow governing equation and the solid deformation by an intrinsic FSI algorithm. Thus, the fluid and solid domains share a common interface with a conformal mesh, i.e., each node of the interface is shared by the fluid and the structure and, therefore, it is not necessary to interpolate data. The displacement of the solid domain results from the continuous forces generated by the fluid, which are unknown a priori and are part of the computation. In this two-way FSI approach, the fluid domain will deform in accordance with the displacements calculated on the solid domain. Of course, the physics and the numerics involved on both sides of the fluid–solid interface differ; however, it is necessary to ensure the continuity of the displacements and of the velocity, as well as the equilibrium of stresses, i.e.,

$$\mathbf{u} = \mathbf{u}_s \quad \text{and} \quad \boldsymbol{\tau}\cdot\mathbf{n} = \boldsymbol{\tau}_s\cdot\mathbf{n} \quad \text{on} \quad S_s(\mathbf{x},t)\,, \tag{8}$$

where $\mathbf{u}$ and $\mathbf{u}_s$ are the fluid and the solid (nondimensional) velocity fields, respectively, $\boldsymbol{\tau}$ and $\boldsymbol{\tau}_s$ the corresponding stress tensors (see below), S_s is the moving fluid–solid interface, with $\mathbf{x}$ and t the dimensionless position vector and time, respectively, and $\mathbf{n}$ the unit vector normal to this surface. In the fluid side the code solves the incompressible Navier–Stokes equations,

$$\boldsymbol{\nabla}\cdot\mathbf{u} = 0\,, \quad \frac{\partial\mathbf{u}}{\partial t} = -\mathbf{u}\cdot\boldsymbol{\nabla}\mathbf{u} + \boldsymbol{\nabla}\cdot\boldsymbol{\tau}\,, \quad \boldsymbol{\tau} = -p\mathbf{I} + \frac{2}{Re}\left[\boldsymbol{\nabla}\mathbf{u} + (\boldsymbol{\nabla}\mathbf{u})^T\right]\,, \tag{9}$$

where $\boldsymbol{\tau}$ is the nondimensional stress tensor, scaled with ρU^2, with p the nondimensional pressure field and $\mathbf{I}$ the unit tensor. For the structural equation of the solid, but deformable body it is assumed linear isothermal and isotropic elasticity for the stress–strain law (e.g., Long (1961)), which in nondimensional form can be written as

$$\frac{\rho_s}{\rho}\frac{\partial^2\boldsymbol{\chi}}{\partial t^2} = \boldsymbol{\nabla}\cdot\boldsymbol{\tau}_s\,, \quad \boldsymbol{\tau}_s = S'\left\{\frac{1}{2}\left[\boldsymbol{\nabla}\boldsymbol{\chi} + (\boldsymbol{\nabla}\boldsymbol{\chi})^T\right] + \frac{\nu}{(1-2\nu)}(\boldsymbol{\nabla}\cdot\boldsymbol{\chi})\mathbf{I}\right\}\,,$$
$$S' = \frac{E}{(1+\nu)\rho U^2}\,, \tag{10}$$

where $\boldsymbol{\chi}(\mathbf{s},t) = \mathbf{X}(\mathbf{s},t) - \mathbf{X}(\mathbf{s},0)$ is the displacement vector, with $\mathbf{X}$ the position vector attached to the solid body, defined in terms of the vector variable $\mathbf{s}$ that parametrizes the body, ν is Poisson's ratio, and the time derivative is here a Lagrangian derivative. The nondimensional parameter S' in Cauchy's stress tensor $\boldsymbol{\tau}_s$ is related to the stiffness ratio S defined in (3) for a two-dimensional thin foil. In this last case, one commonly simplifies the problem by using equations averaged across the small thickness of the foil ϵ, so that $\mathbf{s}$ is reduced to just a scalar s that parametrizes the foil's centerline, as described in Section 2 above, and the effect of Poisson's ratio ν is negligible. Such bending beam approximation is used in Section 5 below to derive analytical solutions of the Euler–Bernoulli beam equation, a linear approximation valid only for small displacements of the foil. But it must be stressed that the numerical results obtained with Eq. (10) are valid for any arbitrary displacement of the foil, provided that it behaves as an elastic solid governed by Cauchy's stress law. Other nonlinear beam approximations to model the foil deflection can also be derived from Eq. (10), like, for instance, the nonlinear beam formulation used by Olivier and Dumas (2016), which is not limited to small deflections of the foil as the Euler–Bernoulli beam equation.

Eq. (10) requires that boundary conditions be given in terms of displacement or in terms of force on the solid body surface S_s. In the present FSI simulation, where the solid is in contact with a surrounding fluid, continuous forces originating from the fluid are assigned as boundary conditions, which must satisfy the conditions (8). To solve this equation numerically a finite element method is used, where the structure is discretized as an assembly of discrete regions (elements) connected at a finite number of points, or nodes. In the present 2D case these elements are triangles or quadrilaterals. With this discretization, Eq. (10) is transformed into a system of linear algebraic equations for the displacements of the nodes, χ_i, which can formally be written as

$$[M]\{\ddot{\chi}(t)\} + [K]\{\chi(t)\} = \{f(t)\}\,, \tag{11}$$

where $[M]$ and $[K]$ are the structural mass matrix and the stiffness matrix, respectively, while $\{\ddot{\chi}(t)\}$ and $\{\chi(t)\}$ are the vectors of nodal accelerations and displacements, respectively. $\{f(t)\}$ is the applied load vector resulting from the external (continuous or nodal) forces applied on the boundary of the solid body. In particular, in the present FSI simulation, they incorporate the forces originating from the fluid motion, which are obtained by solving the flow Eqs. (9) simultaneously at each time step. The additivity property allows the integration in Eq. (11) to be performed at the level of each individual element in order to obtain local mass and stiffness matrices, which are subsequently assembled into the total mass and stiffness matrices of the linear system. After this assembly is completed, displacement boundary conditions, such as those corresponding to the heaving motion at the pivot point, are applied by removing the corresponding unknowns and equations from the system. For numerically solving the finite element semi-discrete equation of motion (11) the Newmark method (Newmark, 1959), available in Fluent, is used. The method is unconditionally stable with any positive amplitude decay factor γ; we use $\gamma = 0.2$. We have enabled the implicit mesh update scheme during each time step, with a motion-relaxation parameter of 0.1 and residual-criteria of 10^{-5} in both spatial directions.

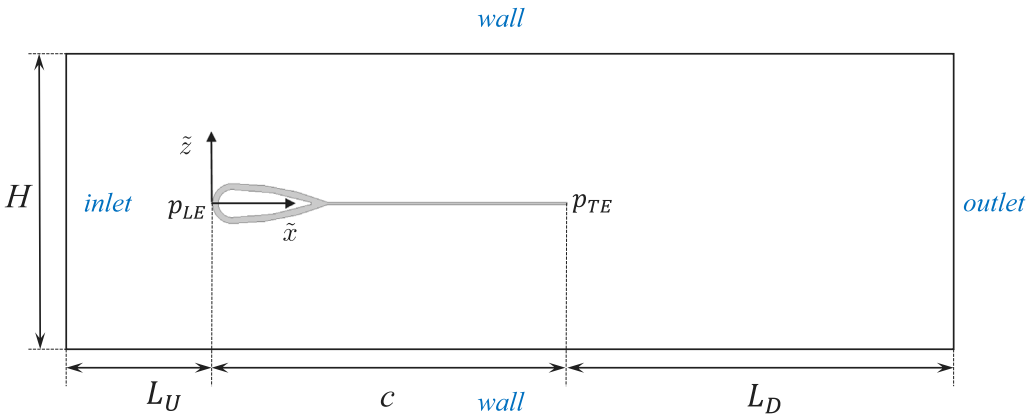

Fig. 2. Teardrop/flat plate foil and computational domain used to compare with experimental results by Heathcote and Gursul (2007) (dimensional quantities).

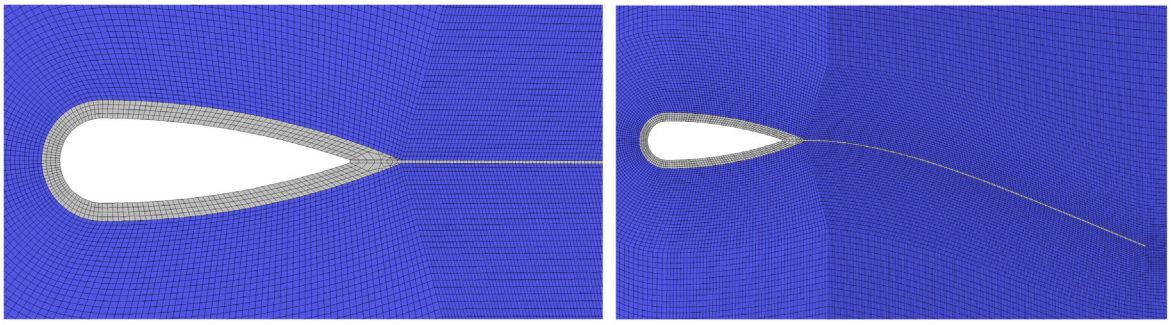

Fig. 3. (a) Detail of the teardrop/flat plate foil with mesh#1. The tail has just one cell across its thickness ($\varepsilon = 0.25$ mm). (b) Mesh deformation at $t/T = 0.75$ (see main text for the values of the flow and structural parameters).

To solve the incompressible and two-dimensional flow around the body, the governing Eqs. (9) are discretized and solved using also the finite volume-based solver implemented in Ansys -Fluent v20.2. Transient, pressure-based, coupled solver with absolute velocity formulation are the settings for the solution of all the numerical simulations. The least-squares cell based method is applied for calculating the gradients of the transport quantities on the faces of the cells. The other spatial discretization methods in the simulations are second order for the pressure term, and second-order upwind for continuity and momentum equations. The explicit relaxation factors of pressure and momentum are set at 0.75 to ensure the stability of the numerical method. First-order implicit formulation is applied for discretizing the temporal derivatives to ensure stability with coupling FSI. At each time step the convergence was stopped once the absolute residuals values 10^{-3} and 10^{-5} for continuity and momentum quantities, respectively, were fulfilled. The simulations are initialized with an unsteady solution with the body at rest. The harmonic motion of the body at the pivot point was written in a User Defined Function (UDF), which is a C^{++} program compiled in Fluent. For the dynamic mesh we used to smooth the mesh the boundary distance diffusion method with a diffusion parameter 1.75. The algebraic multi-grid with the conjugate gradient for pre-conditioning was used for stabilizing the dynamic mesh. In parallel computing with 16 processors intel E5-2670 at 2.6 GHz, 64 GB of RAM memory, and InfiniBand interconnection of 54 Gbits per second, each FSI case took around a week.

For the Reynolds number 10 000 used in most of the computations reported in this work we find that the 2D flow remains laminar, as also shown by Olivier and Dumas (2016) in a similar FSI problem solved numerically using the OpenFoam package (see Section 4.1 below for a comparison with some results from these authors).

4. Validation and grid convergence

4.1. Validation with previous experimental numerical results

To validate the numerical method developed for solving the FSI problem in Ansys -Fluent we compare with experimental results by Heathcote and Gursul (2007). These authors used a teardrop/flat plate design for the foil (see Fig. 2), with chord $c = 90$ mm and 300 mm span. The plate was a sheet of steel of uniform thickness, modulus of elasticity 2.05×10^{11} N/m^2, and length $2c/3$. The teardrop element, with the remaining $c/3$ chord length, was made of solid aluminum and a thickness of 10 mm, so it behaved practically as a rigid body. The flexibility of the plate was varied modifying its thickness ε. In particular, we consider here the case with $\varepsilon/c = 0.56 \times 10^{-3}$. The experiments were made in water at different Reynolds numbers. We select here the case $Re = 9\,000$ for which Heathcote and Gursul (2007) provide a larger variety of experimental results. In our numerical simulations we select the same solid materials (i.e. aluminum for the teardrop element and steel for the plate, with thickness $\varepsilon/c = 0.56 \times 10^{-3}$) and chord length $c = 90$ mm, so it results $U = 0.1$ m/s and $\varepsilon = 0.25$ mm (see Fig. 3(a) for a detail of the plate close to the teardrop junction). The corresponding values of R and S for the flexible plate were $R = 0.0044$ and $S = 3.57$. Finally, an oscillatory heaving motion like (1) is imposed to the head of the foil with $h_0 = 0.3889$ (i.e., $\tilde{h}_0 = 17.5$ mm) and variable frequency. The most detailed comparisons are made with a frequency corresponding to $St = 0.34$.

The dimensions of the computational domain are (see Fig. 2) $H/c = 4.23$, corresponding to the width of the water tunnel test section in Heathcote and Gursul (2007), $L_U = 2c$ upstream of the foil and $L_D = 10c$ downstream. As shown by the grid convergence analysis described below, these last two lengths are large enough to

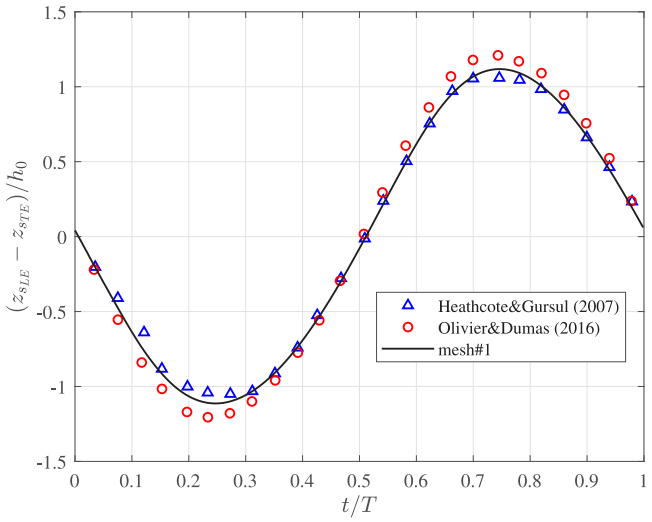

Fig. 4. Relative displacement between leading and trailing edges for $Re = 9\,000, h_0 = 0.389, St = 0.34$ and $\epsilon/c = 0.56 \times 10^{-3}$ (continuous line) compared with experimental results from figure 16 of Heathcote and Gursul (2007) (triangles) and numerical results (Navier–Stokes model) from figure 8 of Olivier and Dumas (2016) (circles).

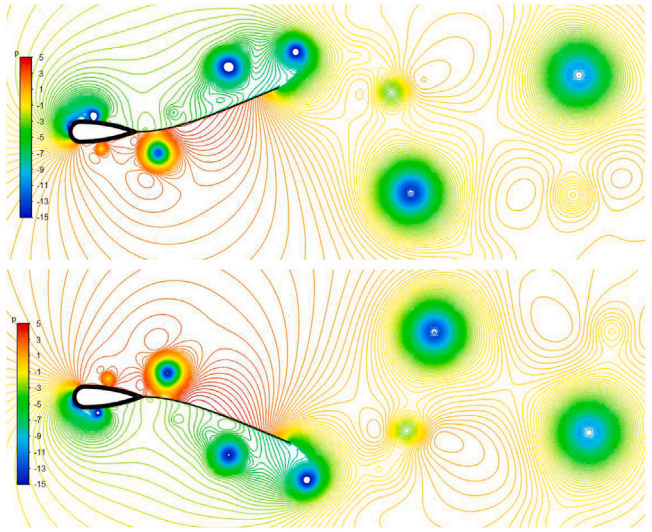

Fig. 5. Contours of dimensionless pressure at $t/T = 0.25$ (top) and $t/T = 0.75$ (bottom).

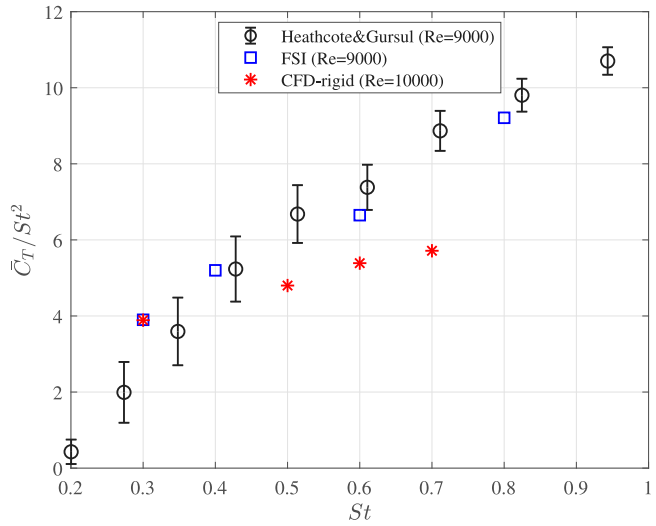

Fig. 6. Time-averaged thrust coefficient computed for several values of St for $Re = 9\,000, h_0 = 0.389$ and $\epsilon/c = 4.23 \times 10^{-3}$ (squares) compared with experimental data from figure 10(a) of Heathcote and Gursul (2007) (circles, with error bars from their force measurement uncertainty). Also included are some numerical results for a rigid plate with the same h_0 and $Re = 10\,000$.

get very accurate results. Furthermore, doubling these distances in the simulations did not show appreciable differences in the results, but a computational time about 75% higher. Transient numerical simulations were made with three different structured grids of quadrilaterals cells: mesh#0 (coarse) with 216 114 cells, 150 in the tail and a time step $\Delta t/T = 0.003$; mesh#1 (medium) with 430 004 cells, 212 in the tail (see Fig. 3) and $\Delta t/T = 0.0015$; mesh#2 (fine) with 857 023 cells, 300 in the tail and $\Delta t/T = 0.00075$. This grid refinement series has been constructed multiplying by $\sqrt{2}$ the number of cells in each spatial direction. We kept the CFL number below 10 in all the numerical simulations. The grid convergence study shows that with mesh#1 one already reaches mesh independency of the results (see Section 4.2 below). It is worth noticing that the use of a fully structured mesh improves notably the convergence of the numerical results at each time step, because the deformed grid remains structured, as it can be observed in Fig. 3(b) for $t/T = 0.75$ after a periodic solution has been reached (as aforementioned, the computations are started from the unsteady flow with the body at rest).

Fig. 4 compares our numerical results for the relative displacement between leading and trailing edges with the experimental results of Heathcote and Gursul (2007). The discrepancies with the experimental data is always smaller than 5%. The figure also plots numerical results obtained by Olivier and Dumas (2016) for the same case using the OpenFoam package. The deflection reaches a strictly periodic state, with maximum deflection at $t/T = 0.25$, when the leading edge of the foil is at its lowest position, and at $t/T = 0.75$, with the leading edge at the highest position [shown in Fig. 3(b)]. The corresponding flow is also periodic, as shown by the computed pressure fields at these two instants of time within a cycle plotted in Fig. 5.

Finally, Fig. 6 compares the time-averaged thrust coefficients computed numerically with the present FSI numerical method for several values of the Strouhal number for the same Re and h_0, but for a larger thickness (and, therefore, stiffness) of the plate, $\epsilon/c = 4.23 \times 10^{-3}$, with the experimental data by Heathcote and Gursul (2007). All the numerical results agree quite well with the experimental ones within the experimental uncertainty. For reference sake we also include in Fig. 6 some results for a rigid plate at $Re = 10\,000$ (se Section 4.2 below). For small Strouhal numbers the results practically coincide with those of the flexible plate, but as St increases the thrust of the flexible plate becomes larger, as expected.

4.2. Grid convergence analysis for a flexible flat plate

The present numerical study about the FSI of a heaving hydrofoil is performed with a 2D flexible flat plate pivoting at the leading edge. To that end we select a plate of chord length $c = 90$ mm and thickness $\epsilon = 0.4$ mm. For the prescribed heaving motion at the leading edge we include there a small circular head of radius 0.9 mm, of the same material as the thin plate, but with a hollow square region inside where the harmonic motion (1) is imposed through a UDF in Ansys-Fluent (see Fig. 7; the size of the square size is 0.65 mm, and the pivot point location is actually at $a = -0.98$ instead of -1). We select the solid material properties such that $R = 0.05$ and $S = 50$, and the flow velocity and fluid properties for $Re = 10\,000$. Since the chord length is the same as in the example considered above, we use the same computational domain (see Fig. 2).

The grid convergence analysis is made with $h_0 = 0.05$ and two sufficiently high reduced frequencies, $k = 5$ and $k = 10$ (corresponding

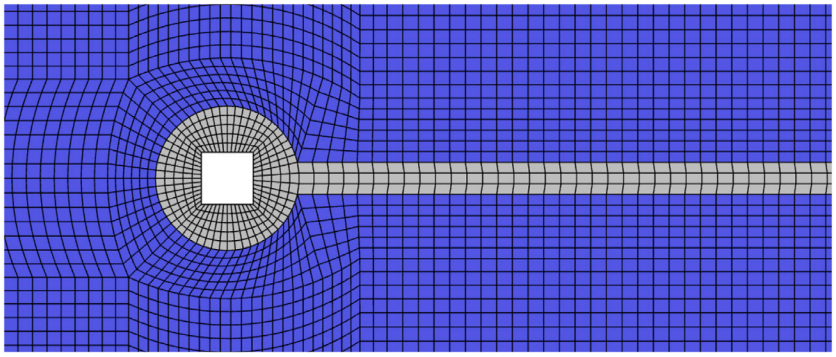

Fig. 7. Detail of the leading edge of the plate and the structured mesh#1.

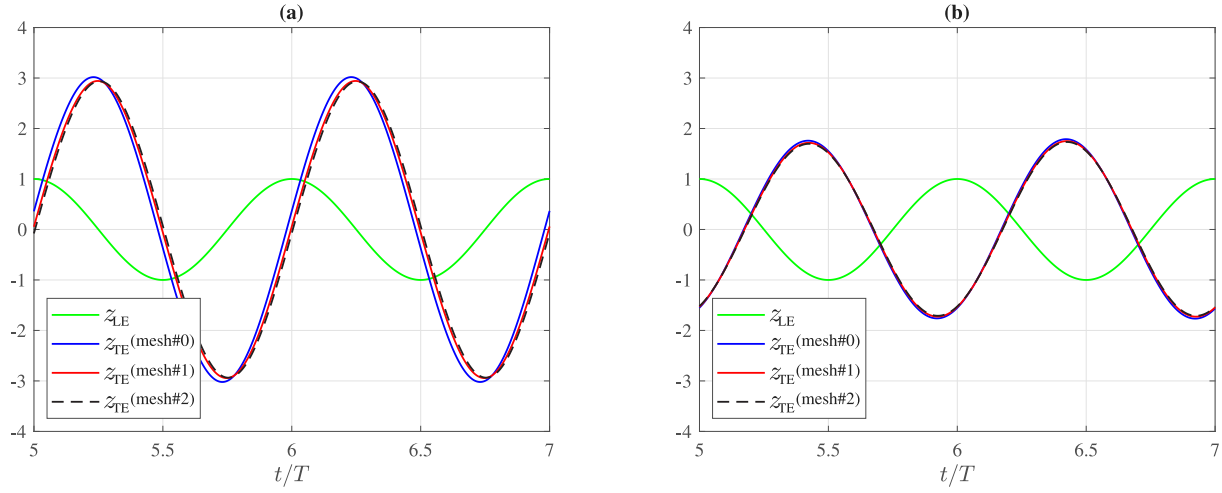

Fig. 8. Evolution of the trailing edge amplitude z_{TE}, normalized with h_0, obtained numerically with the three meshes, compared with the leading edge position, z_{LE}, also normalized with h_0, for $k = 5$ (a) and $k = 10$ (b). $Re = 10\,000$, $h_0 = 0.05$.

to $St = 0.08$ and $St = 0.16$, respectively). We follow a similar procedure to that described above, selecting three different structured grids of quadrilaterals cells: mesh#0 (coarse) with 237 164 cells, 300 in the plate, with two cells across its thickness, and a time step $\Delta t/T = 0.002$; mesh#1 (medium) with 470 298 cells, 450 in the plate, with three cells across its thickness (see Fig. 7) and $\Delta t/T = 0.001$; mesh#2 (fine) with 952 646 cells, 637 in the plate, with four cells across its thickness, and $\Delta t/T = 0.0005$. The CFL was less than 10 in all the numerical simulations.

Fig. 8 shows the position of the trailing edge as a function of time obtained numerically using the three different meshes for both values of k, representing also the leading edge position for reference sake. For the larger frequency ($k = 10$) the results are practically the same with the three different grids. For $k = 5$, which, as it will be seen in Section 6 below is close to the natural frequency of the FSI system for the present values of R, S and a, the results with the coarse grid (mesh#0) present small discrepancies in relation to those from the finer grids, but the results with meshes #1 and #2 are practically the same. It must be noted that the trailing edge amplitude for $k = 5$ is about three times that of the prescribed motion at the leading edge, while for $k = 10$ it is just slightly larger. Consequently with this grid convergence analysis we shall use mesh#1 for all the numerical computations reported below.

5. Analytical solution in the inviscid linear limit

For a solid body of very small thickness ϵ, if the amplitude of the prescribed heaving motion is small compared to the chord length ($h_0 \ll 1$), and the stiffness of the foil is sufficiently large so that the chordwise deflection amplitude in relation to the rigid foil is also very small compared to c, the thin foil may be considered to be on the plane $z = 0$ in first approximation, i.e., with the parameter s along the foil centerline coinciding with the coordinate x, which extends from $x = -1$ to $x = 1$ if the effect of Poisson's ratio is neglected. Thus, the solid motion is just governed by the Euler–Bernoulli beam equation, which in the present dimensionless variables and for an inviscid fluid can be written as (e.g., Moore, 2017; Fernandez-Feria and Alaminos-Quesada, 2021a)

$$2R\frac{\partial^2 z_s}{\partial t^2} + \frac{2}{3}\frac{\partial^2}{\partial x^2}\left(S\frac{\partial^2 z_s}{\partial x^2}\right) = \Delta p + C_{Li}\delta(x-a) - 2C_{Mi}\delta'(x-a)\,, \qquad (12)$$

where $z_s(x,t)$ is the displacement in the z direction of the centerline of the foil , $\Delta p(x,t) = p^-(x,t) - -p^+(x,t)$ is the pressure difference between the lower and upper sides of the foil, scaled with ρU^2 as before. To this distributed pressure force exerted on the foil by the moving fluid, we have added to Eq. (12) a punctual force and a punctual moment actuating locally at the pivot point $x = a$. Thus, $C_{Li}(t)\delta(x-a)$ is the dimensionless force per unit span, scaled with $\rho U^2 c/2$, that generates the prescribed heaving motion (1), where C_{Li} has to be computed as a part of the solution of the present problem and where $\delta(x-a)$ is Dirac's delta function centered at $x = a$. On the other hand, $-2C_{Mi}(t)\delta'(x-a)$ is the torque per unit span, scaled with $\rho U^2 c^2/2$, actuating locally at $x = a$ to avoid generating any pitching motion of the foil about the pivot point by the application of the punctual force $C_{Li}(t)\delta(x-a)$, where C_{Mi} has also to be computed as a part of the solution of the present problem and where $\delta'(x-a)$ is the derivative of Dirac's delta function at $x = a$ (note that the torque thus defined is positive when counterclockwise). The dimensionless quantities R and S, defined in (3), are in general functions of x through $\rho_s(x)$, $\epsilon(x)$ and $E(x)$.

We proceed as in Fernandez-Feria and Alaminos-Quesada (2021a) by assuming the simplest flexural deflection $z_s(x,t)$ that allows to relate

it to the stiffness S of the foil, which for constant S, and in absence of pitching motion, is given by a quartic polynomial such as

$$z_s(x,t) = h(t) + (x-a)^2 d(t) - (x-a)^3 \frac{2d(t)}{3(1-a)} + (x-a)^4 \frac{d(t)}{6(1-a)^2} . \quad (13)$$

This displacement of the foil represents a heaving motion $h(t)$, here prescribed at $x = a$, combined with a flexural deflection $d(t)$, also about $x = a$, and with a free tailing edge ($\partial^2 z_s/\partial x^2 = \partial^3 z_s/\partial x^3 = 0$ at $x = 1$). With this minimal expression for the deflection of the foil one can obtain $d(t)$ by just taking the first three moments of the Euler–Bernoulli equation (12), which is obtained together with the force and torque, C_{Li} and C_{Mi}, necessary to generate the forced heaving motion $h(t)$ and to suppress any pitching motion about $x = a$, respectively, for given R and S. As shown in Fernandez-Feria and Alaminos-Quesada (2021a) and obtained analytically below, this lowest order approach for the flexural deflection of the foil captures almost exactly the first resonant frequency of the system, but not the subsequent ones, so that it is limited to frequencies below the second natural frequency of the system. However, as shown by Alben (2008), the maximum possible thrust is always achieved by the flexible foil operating at or near the first natural mode, so that it is the most relevant one from the point of view of the propulsive performance. To capture higher resonant modes requires more terms in (13) than those considered here, and the solution has to be obtained numerically (e.g., Paraz et al., 2016; Moore, 2017; Floryan and Rowley, 2018; Tzezana and Breuer, 2019).

Thus, substituting (13) into (12) and integrating between $x = -1$ and $x = 1$, and then integrating that equation multiplied by $x - a$ and by $(x-a)^2$, one obtains the following three equations:

$$m\ddot{h} + J_a\ddot{d} + \frac{16}{3(1-a)^2} S\, d = C_L + C_{Li} , \quad (14)$$

$$m(x_0 - a)\ddot{h} + J_d\ddot{d} - \frac{16a}{3(1-a)^2} S\, d = 2\left(C_M + C_{Mi}\right) , \quad (15)$$

$$I_a\ddot{h} + K_d\ddot{d} + \frac{16}{3}\frac{a^2+\frac{1}{3}}{(1-a)^2} S\, d = C_F , \quad (16)$$

where the dots represent time derivatives. In these expressions,

$$C_L(t) = \int_{-1}^{1} \Delta p(x,t)dx , \quad C_M(t) = \frac{1}{2}\int_{-1}^{1} (x-a)\Delta p(x,t)dx ,$$
$$C_F(t) = \int_{-1}^{1} (x-a)^2 \Delta p(x,t)dx , \quad (17)$$

are the (dimensionless) lift, moment and flexural torque, respectively, exerted on the foil by the pressure forces of the surrounding fluid; the location of the foil's center of mass x_0, the dimensionless mass m, the dimensionless moment of inertia about $x = a$, I_a, and all the other dimensionless moments about the pivot point, are defined as follows:

$$m = 2\int_{-1}^{1} R dx = 4R , \quad (18)$$

$$m(x_0 - a) = 2\int_{-1}^{1} (x-a)R dx = -4aR , \quad x_0 = 2\int_{-1}^{1} xR dx \quad (19)$$

$$I_a = 2\int_{-1}^{1} (x-a)^2 R dx = 4R\left(\frac{1}{3} + a^2\right) , \quad (20)$$

$$J_a = 2\int_{-1}^{1}\left[(x-a)^2 - \frac{2}{3}\frac{(x-a)^3}{1-a} + \frac{(x-a)^4}{6(1-a)^2}\right] R dx$$
$$= 2R\left[a^2 - \frac{2}{3}a - \frac{1}{3} + \frac{16}{15(1-a)^2}\right] , \quad (21)$$

$$I_d = 2\int_{-1}^{1} (x-a)^3 R dx = -4Ra\left(1 + a^2\right) , \quad (22)$$

$$J_d = 2\int_{-1}^{1}\left[(x-a)^3 - \frac{2}{3}\frac{(x-a)^4}{1-a} + \frac{(x-a)^5}{6(1-a)^2}\right] R dx$$
$$= 2R\frac{-12 - 93a + 60a^2 - 110a^3 + 120a^4 - 45a^5}{45(1-a)^2} , \quad (23)$$

$$K_d = 2\int_{-1}^{1}\left[(x-a)^4 - \frac{2}{3}\frac{(x-a)^5}{1-a} + \frac{(x-a)^6}{6(1-a)^2}\right] R dx$$
$$= 2R\frac{141 + 168a + 1281a^2 - 1120a^3 + 1015a^4 - 840a^5 + 315a^6}{315(1-a)^2} , \quad (24)$$

where the expressions on the right-most hand sides correspond to constant R, i.e., when the center of mass coincides with the center of the foil, $x_0 = 0$.

For an harmonic motion of the foil like (1), applied at $x = a$, one may assume

$$d(t) = \mathrm{Re}\left[d_m e^{i(kt+\psi)}\right] , \quad (25)$$

where d_m and ψ are the flexural deflection amplitude and phase shift in relation to the heaving motion, respectively. Using these expressions of $h(t)$ and $d(t)$ in the motion of the foil (13), the coefficients $C_L(t)$, $C_M(t)$ and $C_F(t)$ have been obtained analytically in the linear inviscid limit for arbitrary values of h_0, d_m, ψ, a and k in Fernandez-Feria and Alaminos-Quesada (2021b) (see also Alaminos-Quesada and Fernandez-Feria, 2020, for a more complete description of the vortex impulse theory on which the derivation is based, but using a quadratic polynomial for z_s instead of (13)). These expressions are summarized in Appendix A for easy reference.

Eq. (16), together with the expression (A.3) for C_F and the kinematics given by (1) and (25), constitutes an algebraic equation for the flexural deflection amplitude d_m and the phase shift ψ. These quantities are obtained in terms of the heave amplitude h_0, the reduced frequency k, the pivot and center of mass locations, a and x_0, the stiffness and mass ratio of the foil, S and $R(x)$. Once the flexural deflection has been obtained, Eqs. (14)–(15), together with (A.1) for C_L and (A.2) for C_M, yield the input lift C_{Li}, necessary to generate the prescribed heaving motion and, therefore, to compute the input power and the corresponding efficiency of the system, and the input torque C_{Mi} necessary to avoid any pitching motion about $x = a$.

From Eq. (16), the solution for the flexural deflection can formally be written as

$$\frac{d_m}{h_0} = \left|\frac{b}{A}\right| , \quad \psi = \arg\left(\frac{b}{A}\right) , \quad (26)$$

with

$$A = -K_d k^2 + \frac{16}{3}\frac{a^2+\frac{1}{3}}{(1-a)^2} S + A^F , \quad b = I_a k^2 + b^F , \quad (27)$$

where the superscript F refers to the contributions from the fluid–structure interaction (i.e., from C_F). Using the expression (A.3) for C_F, these contributions can be written as

$$A^F = \pi\left[A_{f2}k^2 - A_{f1}ik - A_{f0} + C(k)(2a^2 + 2a + 1)\left(A_{g1}ik + A_{g0}\right)\right] , \quad (28)$$

$$b^F = \pi\left(a^2 + \frac{1}{4}\right)k^2 - \pi C(k)(2a^2 + 2a + 1)ik , \quad (29)$$

where A_{f0}, A_{f1}, A_{f2}, A_{g0} and A_{g1} are functions of a defined in Eqs. (A.8)–(A.10) in Appendix A.

In absence of fluid–structure interaction (FSI), i.e., assuming $C_F = 0$,

$$\frac{d_m}{h_0} = \frac{I_a k^2}{\left|\frac{16(a^2+1/3)}{3(1-a)^2} S - K_d k^2\right|} . \quad (30)$$

Thus, the corresponding (first) resonant frequency is

$$k_{r0} = \sqrt{\frac{16(a^2+1/3)S}{3(1-a)^2 K_d}}$$
$$= \sqrt{\frac{280(1+3a^2)S}{(141 + 168a + 1281a^2 - 1120a^3 + 1015a^4 - 840a^5 + 315a^6)R}} , \quad (31)$$

with the last expression valid for constant mass ratio R, recovering the well known result that the dimensionless natural frequency of a flexible plate is proportional to $\sqrt{S/R}$ (e.g., Floryan and Rowley, 2018), but now with an analytical expression for its dependence on the pivot point

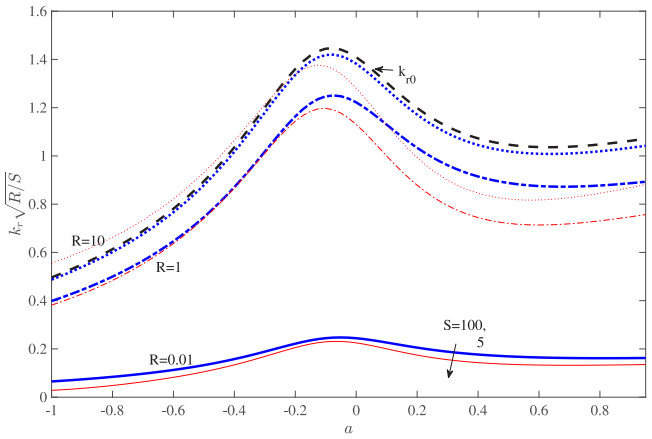

Fig. 9. First natural frequency k_r that minimizes $|A|$ vs. a for $S = 100$ (thick blue lines) and $S = 5$ (thin red lines) and three values of R, as indicated, compared with k_{r0} given by (31) (black dashed line). (For interpretation of the references to color in this figure legend, the reader is referred to the web version of this article.)

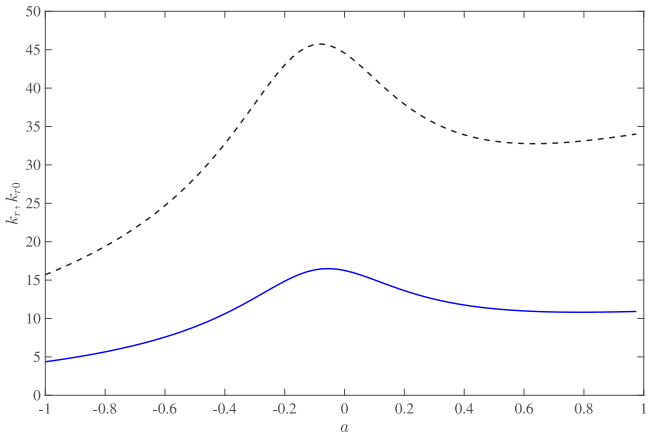

Fig. 10. First natural frequency k_r that minimizes $|A|$ vs. a (continuous line) compared with k_{r0} given by (31) (dashed line) for $S = 50$ and $R = 0.05$.

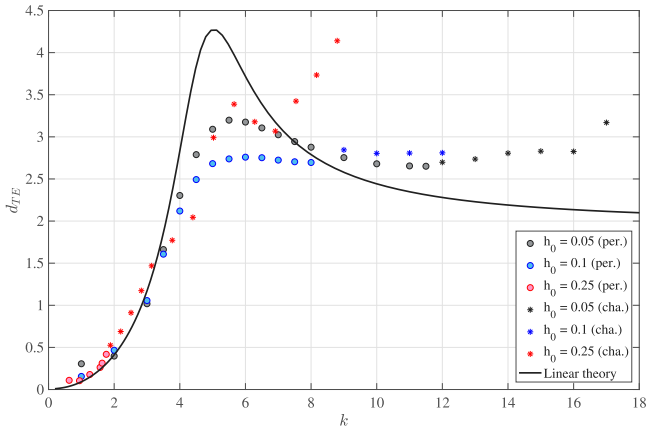

Fig. 11. Flexural deflection amplitude at the trailing-edge vs. reduced frequency from linear theory (line), and from numerical simulations for $Re = 10\,000$ with different values of h_0 (symbols). Circles correspond to periodic numerical solutions and stars to chaotic solutions (which are time-averaged; see the main text). $a = -0.98$, $S = 50$ and $R = 0.05$.

location in the present approximation. For a pivot at the leading edge ($a = -1$), $k_{r0} = \sqrt{35S/(142R)} \simeq 0.496\sqrt{S/R}$, recovering almost exactly the result for the first resonant frequency obtained numerically from a more general inviscid theory by Floryan and Rowley (2018) for $a = -1$.

When the FSI is taken into account, the denominator A of (26) is not longer real, and there is no proper resonant frequency at which d_m becomes singular. But there exists a frequency that maximizes the flexural deflection amplitude d_m, and therefore the thrust force (see Section 6 below), for each set of dimensionless parameters. Since at this frequency, $k = k_r$ say, which corresponds to the minimum value of $|A|$, the maximum of d_m is quite large, it may still be called the (first) resonant, or natural, frequency of the system. Obviously, this frequency tends to the resonant frequency k_{r0} given above for $R \to \infty$, when the FSI becomes negligible. This is shown in Fig. 9, where $k_r\sqrt{R/S}$ is plotted as a function of a for two values of S and three of R. For $R = 10$, k_r that minimizes $|A|$ almost coincide with k_{r0}, particularly for large S.

Once $d(t) = d_m e^{i(kt+\psi)}$ is obtained, Eq. (14) yields the required input lift C_{Li}, and hence the input power coefficient:

$$C_{Pi}(t) = \dot{h}(t) C_{Li}(t)\,. \tag{32}$$

One can also obtain the propulsion coefficient $C_T(t)$ from the resulting flexural deflection motion and the prescribed heaving kinematics (Alaminos-Quesada and Fernandez-Feria, 2020; Fernandez-Feria and Alaminos-Quesada, 2021b). Its time-averaged value [defined in Eq. (6)] can be written as

$$\overline{C}_T = (kh_0)^2 t_h(k) + kh_0 d_m t_{dh}(k,a,\psi) + d_m^2 t_d(k,a)\,, \tag{33}$$

with the functions $t_h(k)$, $t_{dh}(k,a,\psi)$ and $t_d(k,a)$ obtained in Fernandez-Feria and Alaminos-Quesada (2021b) and reproduced in Appendix B for easy reference. For $d_m = 0$ one recovers the mean thrust coefficient $\overline{C}_T^0$ of an otherwise identical rigid foil with the same plunging motion (Fernandez-Feria, 2016, 2017).

Finally, to compute the propulsive (Froude) efficiency (7) one also needs the time-averaged input power coefficient, which can be written as the sum of different contributions:

$$\overline{C}_{Pi} \equiv \overline{\dot{h} C_{Li}} = \overline{C}_{Pi}^0 + \overline{C}_{Pi}^d + \overline{C}_{Pi}^m + \overline{C}_{Pi}^S\,. \tag{34}$$

$\overline{C}_{Pi}^0$ is the FSI contribution from the terms in C_L associated to the heaving motion of the foil as a rigid solid,

$$\overline{C}_{Pi}^0 = \pi (kh_0)^2 \mathcal{F}(k)\,. \tag{35}$$

This contribution obviously coincides with Theodorsen's power coefficient for a purely heaving motion of a rigid foil (Theodorsen, 1935; Garrick, 1936), where $\mathcal{F}$ is the real and imaginary parts of Theodorsen's function C given in Eq. (A.5). The other contribution from the FSI, associated to the flexural deflection motion of the foil (i.e., from terms in C_L containing d), is

$$\overline{C}_{Pi}^d = \pi k h_0 d_m \left[\left(A_{l2}\frac{k^2}{2} - A_{g1} k\mathcal{G} + A_{g0}\mathcal{F} \right) \sin\psi + \left(-A_{l1}\frac{k}{2} + A_{g1} k\mathcal{F} + A_{g0}\mathcal{G} \right) \cos\psi \right], \tag{36}$$

where A_{l1}, A_{l2}, A_{g0} and A_{g1} are functions of a defined in Eqs. (A.6)–(A.10) in Appendix A. The term $\overline{C}_{Pi}^m$ is the contribution from the inertia of the foil,

$$\overline{C}_{Pi}^m = -\frac{k^3 h_0}{2} J_a d_m \sin\psi \tag{37}$$

(note that J_a, given by Eq. (21), depends on R and therefore on m), while $\overline{C}_{Pi}^S$ is the contribution from the stiffness of the foil,

$$\overline{C}_{Pi}^S = \frac{8S}{3(1-a)^2} kh_0 d_m \sin\psi\,. \tag{38}$$

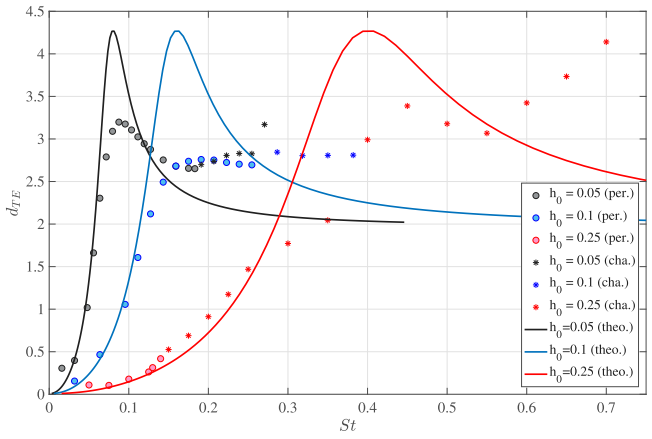

Fig. 12. Same as Fig. 11 but in terms of St instead of k. Now the theoretical curves depend on h_0.

6. Comparison between numerical and theoretical results

One of the main objectives of this work is to compare the above analytical expressions with accurate numerical solutions of the full FSI problem to find out to what extent one can use the analytical predictions to characterize the propulsive performance of a heaving flexible foil. Numerical solutions are very expensive in computational time, so that we consider only selected values of S, R, a and Re for a plate of uniform thickness and density, and vary the frequency k and the heave amplitude h_0 (or the Strouhal number St). In particular, the reported numerical results are for $Re = 10\,000$, and we select a relatively high value of the stiffness, $S = 50$, because the thrust amplification due to flexibility at, or near, the natural frequencies are more important when the stiffness is large enough (Alben, 2008; Dewey et al., 2013; Moore, 2015). The selected value of the mass ratio is small, $R = 0.05$, of greater interest in swimming, rather than in flying, problems (Floryan and Rowley, 2018). The natural frequencies corresponding to these values of R and S are plotted in Fig. 10 as a function of the pivot point location a. Finally, we force the heaving motion at the leading edge, $a = -1$, so that we use the foil configuration for which the grid convergence analysis has been made in Section 4.2. For these values of R, S and a, the natural frequency, $k_r \simeq 4.4$, is well below the resonant frequency *in vacuo* $k_{r0} = 15.7$ (see Fig. 10) due to the smallness of the mass ratio R.

First, we consider the trailing-edge deflection, which in the linear theory is given by

$$z_{TE}(t) = z_s(1,t) = h(t) + \frac{(1-a)^2}{2} d(t)\,. \tag{39}$$

Fig. 11 compares the maximum of the flexural deflection amplitude at the trailing edge in relation to the heaving motion at the leading edge, i.e.,

$$d_{TE} = \frac{max|z_{TE}(t) - h(t)|}{h_0}\,, \tag{40}$$

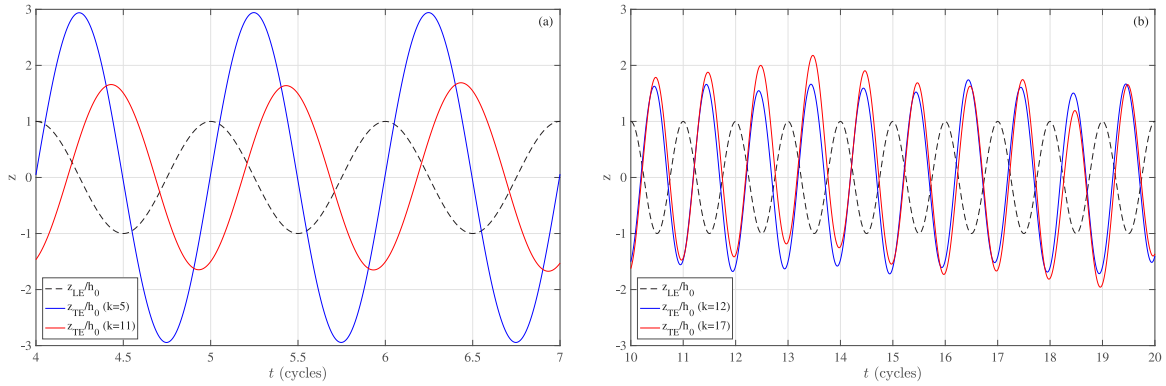

Fig. 13. Evolution of the trailing ledge amplitude computed numerically (continuous lines), compared with the leading edge amplitude (dashed lines), for periodic solutions with $k = 5$ and 11 (a), and for chaotic solutions with $k = 12$ and 17 (b), for the case with $h_0 = 0.05$ plotted in Fig. 11.

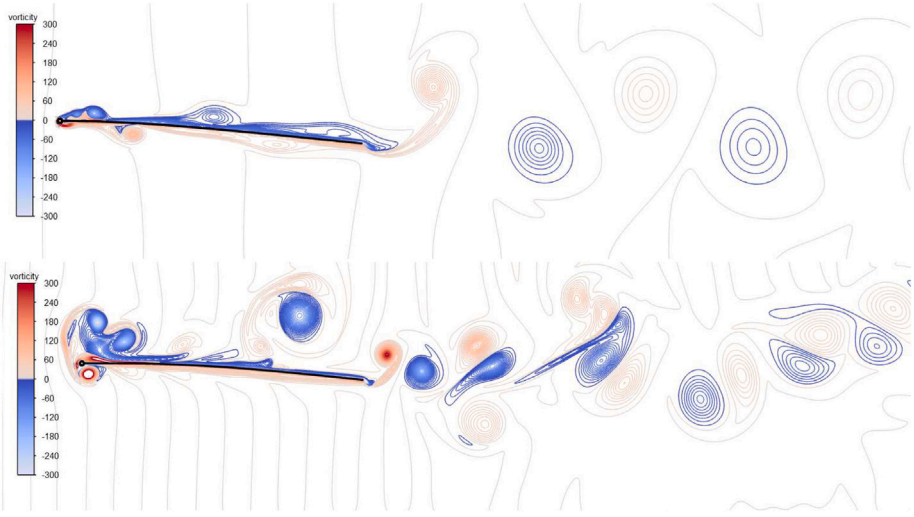

Fig. 14. Snapshots of the nondimensional vorticity field for the cases with $k = 5$ (top) and $k = 17$ (bottom) in Fig. 11 at $t/T = 6.75$ and $t/T = 20$, respectively.

obtained from the linear theory with numerical results as the reduced frequency k is varied. Note that this quantity is obviously zero for a rigid foil. From the linear theory, $d_{TE} = (1-a)^2 d_m/h_0$ and it is independent of the heave amplitude h_0. The numerical results are obtained for $h_0 = 0.05$, 0.1 and 0.25. For sufficiently small amplitude h_0 this figure shows that the linear theory predicts quite accurately the frequency for the maximum deflection amplitude, which roughly coincides with the natural frequency k_r that minimizes $|A|$. However, the theory over-predicts this maximum of d_{TE}, the more so the larger h_0, which was to be expected given its linearity. Note that the linear theory without FSI predicts a singularity of the flexural deflection amplitude at the resonant frequency [see equation (30)]. FSI damps the singularity at this frequency, but not enough since the theory is based on inviscid flow. But it is remarkable that even for a high heave-amplitude as $h_0 = 0.25$, the frequency for the first local maximum of d_{TE} is still well predicted by the linear theory.

This is even more surprising considering that the flow ceases to remain periodic and becomes chaotic above a threshold frequency that decreases rapidly as h_0 increases. This transition is characterized in Fig. 11 by a change in the symbols used for plotting the numerical results: circles for periodic solutions and stars for chaotic solutions. For the lower amplitudes, $h_0 = 0.05$ and 0.1, this transition occurs at k larger than the natural frequency k_r, but for the largest amplitude $h_0 = 0.25$, the transition takes place at a value of k well below k_r. If one plots the results of Fig. 11 in terms of the Strouhal number (2) (see Fig. 12), all the transitions to chaotic solutions take place in a narrow range of St between 0.15 and 0.25, approximately, independently of the heave amplitude.

To better appreciate how the foil motion changes after these transitions, Fig. 13 shows the temporal evolutions of the relative trailing-edge amplitude, $z_{TE}(t)/h_0$, for $h_0 = 0.05$ and four values of k: 5 and 11 (St = 0.08 and 0.175), yielding periodic oscillations, and 12 and 17 (St = 0.19 and 0.27), corresponding to chaotic solutions. When the temporal evolutions are aperiodic, the time-averaged quantities represented in Figs. 11 and 12, and in all the other similar results reported below in this section, are computed over the last ten cycles. Note in Fig. 13 that the trailing-edge amplitude for $k = 5$ is much larger than the rest, since this frequency is very close to the natural frequency (see Fig. 11). The different temporal evolutions in Fig. 13 are of course a consequence of the different flow patterns, as depicted in Fig. 14 for $k = 5$ and $k = 17$ at selected instants of time: The first case shows a spatiotemporal periodic structure associated to a mostly attached flow, while in the second case the flow is no longer attached to the foil and becomes chaotic.

Peaks in trailing-edge deflection amplitude at roughly the natural frequencies produce maxima in the time-averaged thrust coefficient, as shown in Fig. 15 for the same cases considered in Figs. 11 and 12. The theoretical results are computed from (33), but subtracting a constant quasistatic drag $C_{D0} = 0.035$ that corrects the inviscid results to account for viscous effects in a quite simple way (see, e.g., Mackowski and Williamson, 2017; Fernandez-Feria, 2017). This viscous effect is relatively more relevant as $k \to 0$, where the theoretical $\overline{C}_T$ vanishes. Without considering this quasistatic drag, $\overline{C}_T/h_0^2$ from the linear inviscid theory is independent of k (shown as a dashed-and-dotted line in Fig. 15(a), which practically coincide with the curve for $h_0 = 0.25$, since at that large amplitude the effect of C_{D0} is negligible, as $\overline{C}_T$ scales as h_o^2). Similarly to the trailing-edge deflection amplitude, when h_0 is sufficiently small (i.e., for $h_0 = 0.05$ and 0.1 in the present results), the linear theory predicts remarkably well the natural frequency k_r at which $\overline{C}_T$ reaches the first local maximum, but over-predicting its magnitude, the more so the larger the amplitude h_0. Note also that the linear theory for $\overline{C}_T$ fails for large k once the first resonant peak is passed, since it only recovers the first natural mode. The numerical results show that for these high values of k the flow becomes chaotic. But even when h_0 is large enough so that this transition to an aperiodic flow occurs at lower frequencies than the first natural mode, as in the present case with $h_0 = 0.25$, good theoretical predictions are found for $k \lesssim k_r$.

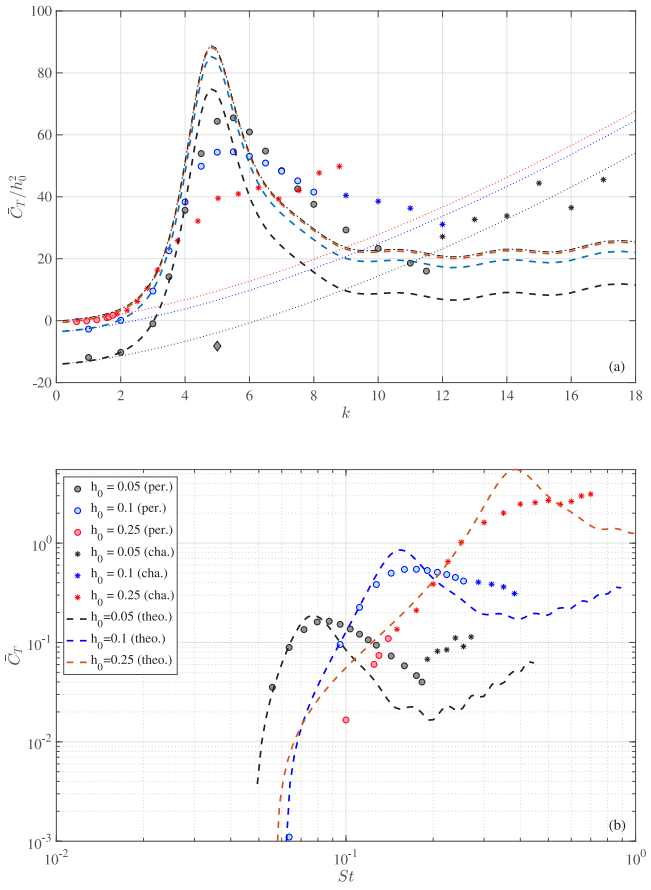

Fig. 15. Time-averaged thrust coefficient for the same cases considered in Figs. 11 and 12, normalized with h_0^2 vs. k in (a) and as a function of St in (b). In the linear theory results, $C_{D0} = 0.035$ has been subtracted in all cases, except in the dashed-and-dotted line in (a) (very close to the red dashed line for $h_0 = 0.25$). Dotted lines in (a) correspond to the theoretical results for rigid foils ($S \to \infty$) with the same values of the rest of parameters, and the diamond ♦ [also in (a)] to the numerical result for a rigid foil with $h_0 = 0.05$ and $k = 5$. (For interpretation of the references to color in this figure legend, the reader is referred to the web version of this article.)

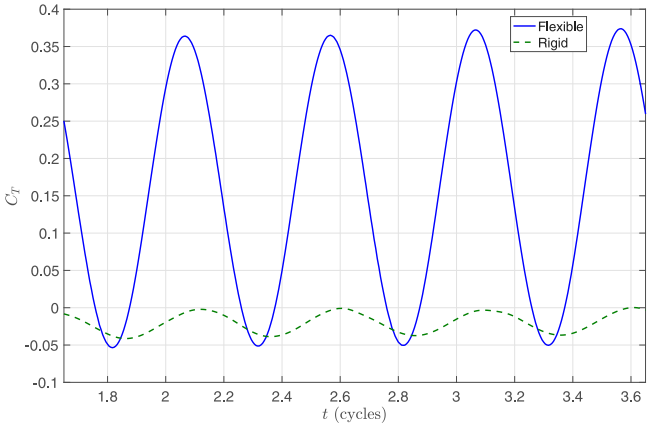

Fig. 16. Comparison between the temporal evolutions of C_T for the flexible ($S = 50$) and the rigid ($S = 5\times10^{11}$) foils when $h_0 = 0.05$ and $k = 5$, and the same values of the remaining parameters ($Re = 10\,000$, $a = -0.98$ and $R = 0.05$).

Also shown in Fig. 15(a) with dotted lines are the theoretical results for an otherwise identical rigid foil, and marked with a diamond the

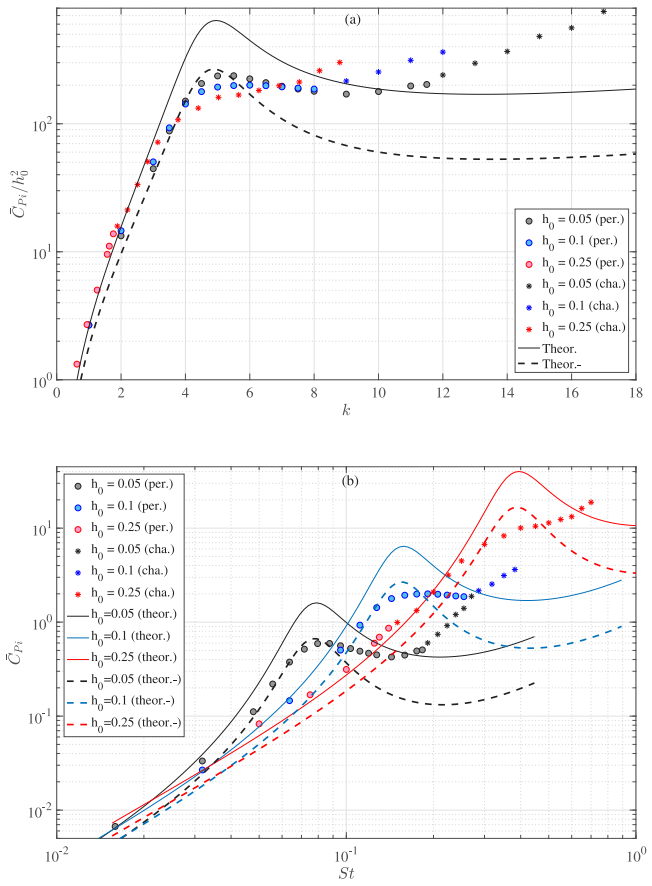

Fig. 17. Time-averaged input power coefficient for the same cases considered in Figs. 11 and 12, normalized with h_0^2 vs. k in (a) and as a function of St in (b). Thin continuous lines are for the theoretical results given by Eq. (34), while dashed lines correspond to the part of $\overline{C}_{Pi}$ only due to the FSI, i.e., $C_{Pi}^F = \overline{C}_{Pi}^0 + \overline{C}_{Pi}^d$.

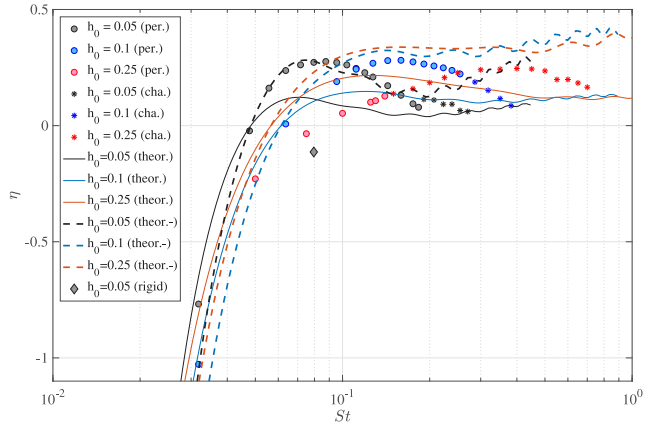

Fig. 18. Propulsive efficiency $\eta = \overline{C}_T/\overline{C}_{Pi}$ vs. Strouhal number corresponding to the $\overline{C}_T$ results plotted in Fig. 15(b) and the $\overline{C}_{Pi}$ given in figure 17(b). The ♦ corresponds to the numerical result for an otherwise identical rigid foil with $h_0 = 0.05$ and $k = 5$.

numerical result for a rigid foil (actually $S = 5 \times 10^{11}$) when $h_0 = 0.05$ and $k = 5$, very close to the resonant frequency k_r. They are included to show the huge thrust enhancement due to flexibility at the natural frequency. Compare, for instance, the diamond with the gray circle for the same k. Actually, the rigid foil at these flapping conditions ($h_0 = 0.05$ and $k = 5$) does not produce net thrust, just drag. This is more clearly appreciated with the temporal evolutions of C_T shown in Fig. 16.

A similar behavior is obtained for the time-averaged input power coefficient (Fig. 17). Now, numerical results only consider the input power associated to the fluid–structure interaction, while the theoretical expression (34) also includes the components of the input power associated to the inertia and stiffness of the foil. Thus, in addition to the linear theory results given by Eq. (34), which are plotted in Fig. 17 as thin continuous lines, we also plot the components associated only to the FSI, i.e.,

$$\overline{C}_{Pi}^F \equiv \overline{C}_{Pi}^0 + \overline{C}_{Pi}^d, \tag{41}$$

as dashed lines. These last curves agree quite well with the numerical results up to the natural frequency even for the highest amplitude $h_0 = 0.25$, in spite of the fact that, as aforementioned, the flow becomes chaotic at much lower frequencies. Note however that the numerical results only present a clear maximum of the input power around the natural frequency for the lowest amplitude considered.

Since the maxima in the thrust and input power are both roughly reached at the natural frequency, it is not clear whether the Froude efficiency (7) would present a maximum at this frequency or at some other frequency, or indeed no distinguished local maximum at all. Fig. 18, where we plot the propulsive efficiency corresponding to the thrust coefficients given in Fig. 15 and the input power coefficients given in figure 17, shows that the numerical results for η actually do present local maxima roughly at the natural frequency ($k \approx 5$, corresponding to $St \approx 0.08, 0.15$ and 0.4 for $h_0 = 0.05, 0.1$ and 0.25, respectively), while the results from the linear theory do not, except for the lowest amplitude $h_0 = 0.05$. For this h_0 the agreement between the linear theory (considering only the part $\overline{C}_{Pi}^F$ due to FSI, as in the numerical computations) and the numerical results for η is quite remarkable indeed. However, for the higher values of h_0 considered, the linear theory provides just a good estimate of the maximum propulsive efficiency. The maximum computed efficiency for $h_0 = 0.05$ is about 28% at $St \approx 0.08$, which practically coincide with the prediction from the linear theory. It must be noted that for these flapping conditions, the otherwise identical rigid foil does not produce net thrust, and its efficiency is therefore negative (shown in Fig. 18 with a diamond).

7. Conclusion

Accurate numerical results for the propulsive performance of a flexible plunging hydrofoil have been compared to the analytical predictions of linear theory, both considering the fluid–structure interaction. In particular, the theory yields the first natural frequency of the fluid–foil system from just a simple algebraic equation. The optimal propulsive performance obtained numerically, both in terms of thrust enhancement in relation to an otherwise identical rigid foil and of propulsive efficiency, occurs when the foil is operated at a frequency which is quite accurately predicted by the theoretical natural frequency, even for plunging amplitudes which are not so small. However, the magnitude of the thrust force and efficiency are well predicted by the linear theory only for very small amplitudes, as expected, overestimating them as the amplitude increases. Therefore, the natural frequency k_r from the linear theory constitutes a simple and reliable estimation of the optimal frequency for underwater propellers based on flexible plunging hydrofoils, a prediction that may reduce the number of costly numerical computations or expensive experiments. k_r is obtained by just minimizing $|A|$, with A given by Eq. (27). From this equation, Fig. 19 provides, for instance, a convenient chart to select the optimal actuating flapping frequency for a foil of any stiffness ratio S and mass ratio R actuated at the leading edge ($a = -1$), or for a foil with pivot point locations between the leading edge and the mid-chord for a wide range of mass ratios and a given stiffness ratio.

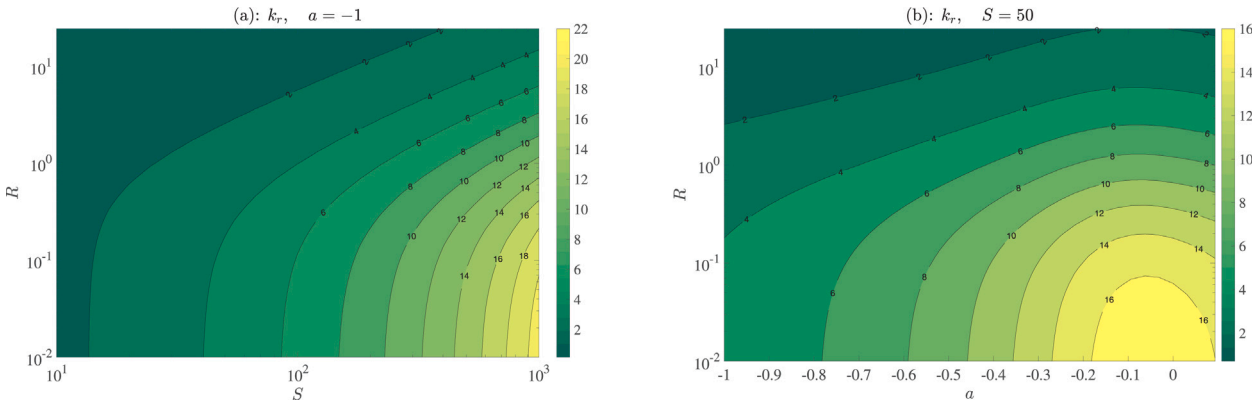

Fig. 19. Contours of natural frequency k_r minimizing $|A|$ in the (S, R) plane for $a = -1$ (a), and in the (a, R) plane for $S = 50$.

CRediT authorship contribution statement

E. Sanmiguel-Rojas: Data curation, Formal analysis, Funding acquisition, Investigation, Methodology, Project administration, Resources, Software, Validation, Visualization, Writing - review & editing. **R. Fernandez-Feria:** Conceptualization, Formal analysis, Funding acquisition, Investigation, Methodology, Project administration, Software, Supervision, Validation, Visualization, Writing - original draft, Writing - review & editing.

Declaration of competing interest

The authors declare that they have no known competing financial interests or personal relationships that could have appeared to influence the work reported in this paper.

Acknowledgments

This research has been supported by the Junta de Andalucía, Spain (Grants UMA18-FEDER-JA-047 and P18-FR-1532), and by the *Ministerio de Ciencia e Innovación* of Spain (Grant PID2019-104938RB-I00). Funding for open access charge: Universidad de Málaga / CBUA. The computations were performed in the Picasso Supercomputer at the University of Málaga, a node of the Spanish Supercomputing Network.

Appendix A. Lift, moment and flexural coefficients from linear potential theory

The following expressions for the coefficients corresponding to the quartic foil's deflection (13) are taken from Fernandez-Feria and Alaminos-Quesada (2021a), but without (passive) pitching motion ($a_0 = 0$):

$$C_L(t) = \pi\left[-\ddot{h} + A_{l2}(a)\ddot{d} + A_{l1}(a)\dot{d}\right] + C(k)\Gamma_0(t)\,, \tag{A.1}$$

$$C_M(t) = \frac{\pi}{2}\left[a\ddot{h} + A_{m2}(a)\ddot{d} + A_{m1}(a)\dot{d} + A_{m0}(a)d\right] - \frac{1}{2}\left(\frac{1}{2} + a\right)C(k)\Gamma_0(t)\,, \tag{A.2}$$

$$C_F(t) = \pi\left[-\left(a^2 + \frac{1}{4}\right)\ddot{h} + A_{f2}(a)\ddot{d} + A_{f1}(a)\dot{d} + A_{f0}(a)d\right] + \left(\frac{1}{2} + a + a^2\right)C(k)\Gamma_0(t)\,, \tag{A.3}$$

where

$$\Gamma_0(t) = -2\pi\left[\dot{h} + A_{g1}(a)\dot{d} + A_{g0}(a)d\right] \tag{A.4}$$

is the quasi-steady (nondimensional) circulation,

$$C(k) = \frac{H_1^{(2)}(k)}{iH_0^{(2)}(k) + H_1^{(2)}(k)} = \mathcal{F}(k) + i\mathcal{G}(k) \tag{A.5}$$

is Theodorsen's function (Theodorsen, 1935), and $H_n^{(2)}(z) = J_n(z) - iY_n(z)$, $n = 0, 1$, Hankel's function of the second kind and order n, related to the Bessel functions of the first and second kind $J_n(z)$ and $Y_n(z)$ (Olver et al., 2010), and where the following functions of a have been defined:

$$A_{l2} = -\frac{13 + 48a^2 - 64a^3 + 24a^4}{48(1-a)^2}\,, \quad A_{l1} = \frac{3 + 12a - 12a^2 + 4a^3}{6(1-a)^2}\,, \tag{A.6}$$

$$A_{m2} = \frac{2 + 25a - 12a^2 + 52a^3 - 64a^4 + 24a^5}{48(1-a)^2}\,, \qquad A_{m1} = \frac{-9 + 12a - 72a^2 + 56a^3 - 16a^4}{24(1-a)^2}\,, \tag{A.7}$$

$$A_{m0} = -\frac{3}{4(1-a)^2}\,, \qquad A_{f2} = -\frac{35 + 32a + 392a^2 - 320a^3 + 496a^4 - 512a^5 + 192a^6}{384(1-a)^2}\,, \tag{A.8}$$

$$A_{f1} = \frac{1 + 8a - 18a^2 + 48a^3 - 32a^4 + 8a^5}{12(1-a)^2}\,, \quad A_{f0} = \frac{7 + 18a}{12(1-a)^2}\,, \tag{A.9}$$

$$A_{g1} = \frac{15 - 48a + 96a^2 - 80a^3 + 24a^4}{48(1-a)^2}\,, \quad A_{g0} = \frac{3 - 24a + 24a^2 - 8a^3}{12(1-a)^2}\,. \tag{A.10}$$

Appendix B. Functions for the theoretical time-averaged thrust coefficient

The functions $t_h(k)$, $t_{dh}(k, a, \psi)$ and $t_d(k, a)$ appearing in the time-averaged thrust coefficient (33) can be written as (Fernandez-Feria and Alaminos-Quesada, 2021b):

$$t_h = -2\mathcal{G}_1\,, \tag{B.1}$$

$$t_{dh} = \left[\pi\left(A_{d0}^I - kA_{d1}^R - D\mathcal{G}\right) - 2A\mathcal{G}_1 k + \frac{3}{2}(E-J)\left(\pi\mathcal{G} - \frac{\mathcal{G}_1 k}{2}\right) - Q\left(\mathcal{F}_1 - \frac{\mathcal{G}_1 k}{2} + \frac{\pi\mathcal{G}}{2}\right)\right]\cos(\psi) + \left[\pi\left(-A_{d0}^R - kA_{d1}^I + D\mathcal{F}\right) - 2A\mathcal{F}_1 k + \frac{3}{2}(E-J)\left(-\frac{\mathcal{F}_1 k}{2} - \pi\mathcal{F}\right) + Q\left(\frac{\mathcal{F}_1 k}{2} + \frac{\pi\mathcal{F}}{2} + \mathcal{G}_1\right)\right]\sin(\psi)\,, \tag{B.2}$$

$$t_d = \frac{\pi}{4}\left\{Q\left[-kA_{d0}^I + 2A_{d0}^R + 2kA_{d1}^I + k^2A_{d1}^R - 2A\mathcal{G}k + D(\mathcal{G}k - 2\mathcal{F}) + (E-J)\left(3\mathcal{F} - \frac{9\mathcal{G}k}{4}\right)\right] +\right.$$

$$k\left(4A+\frac{3E}{2}-\frac{3J}{2}\right)\left[A^I_{d0}-kA^R_{d1}+\mathcal{G}\left(-D+\frac{3E}{2}-\frac{3J}{2}\right)\right] + Q^2\left(\frac{\mathcal{G}k}{2}-\mathcal{F}\right)\Bigg\}. \tag{B.3}$$

The following functions of the pivot point location a and the reduced frequency k are used:

$$Q(a)=2B(a)-2D(a)+3E(a)-3J(a), \tag{B.4}$$

$$A(a)=a^2\left(1+\frac{2a}{3(1-a)}+\frac{a^2}{6(1-a)^2}\right),\quad B(a)=2a\left(1+\frac{a}{1-a}+\frac{a^2}{3(1-a)^2}\right), \tag{B.5}$$

$$D(a)=1+\frac{2a}{1-a}+\frac{a^2}{(1-a)^2},\quad E(a)=\frac{2}{3(1-a)}\left(1+\frac{a}{1-a}\right),\quad J(a)=\frac{1}{6(1-a)^2}; \tag{B.6}$$

$\mathcal{F}(k)$ and $\mathcal{G}(k)$ are the real and imaginary parts of Theodorsen's function (A.5), and likewise $\mathcal{F}_1(k)$ and $\mathcal{G}_1(k)$ in relation to the complex function

$$C_1(k)=\frac{\frac{1}{k}e^{-ik}}{iH_0^{(2)}(k)+H_1^{(2)}(k)}; \tag{B.7}$$

$A^R_{dj}(k,a)$ and $A^I_{dj}(k,a)$, $j=0,1$, are the real and imaginary parts of the functions

$$A_{d0}(k,a)=-Bg_0+D[1+2g_1(k)-C(k)]-E\left[\frac{1}{2}+3g_2+\frac{C}{2}\right] + J\left[4g_3+\frac{C}{2}+\frac{C_3}{k}\right], \tag{B.8}$$

$$A_{d1}(k,a)=Ag_0-Bg_1+Dg_2-E\left[g_3-\frac{i}{2k}C\right]+J\left[g_4-\frac{C_2}{2k}\right], \tag{B.9}$$

with

$$C_2(k)=\frac{H_2^{(2)}(k)}{iH_0^{(2)}+H_1^{(2)}(k)},\quad C_3(k)=\frac{Y_0(k)-iJ_2(k)+iH_1^{(1)}(k)}{iH_0^{(2)}+H_1^{(2)}(k)}, \tag{B.10}$$

$$g_0(k)=\frac{-2i}{\pi}C_1(k),\quad g_1(k)=-\frac{2}{\pi k}(1+ik)C_1(k)-\frac{i}{k}C(k), \quad g_2(k)=-\frac{1}{k}C_2(k)+\left(\frac{2i}{k^2}-\frac{2+ik}{k}\right)C_1(k), \tag{B.11}$$

$$g_3(k)=\frac{3Y_2(k)-kY_1(k)+iJ_3(k)-iJ_2(k)}{k^2\left[iH_0^{(2)}+H_1^{(2)}(k)\right]}+\frac{6}{\pi k}(1+ik)\left(\frac{2}{k^2}-1\right)C_1(k), \tag{B.12}$$

$$g_4(k)=\frac{1}{iH_0^{(2)}+H_1^{(2)}(k)}\left\{\frac{1}{k^2}\left[kJ_4(k)-3J_3(k)\right]+\frac{ik}{4}G^{2,0}_{1,3}\left(\frac{k^2}{4}\middle|\begin{matrix}-\frac{3}{2}\\ -3,0,-\frac{1}{2}\end{matrix}\right)\right\} + \frac{2}{\pi}\left[\frac{24}{k^4}(k-i)-\frac{4}{k^2}(k-3i)-i\right]C_1(k), \tag{B.13}$$

where J_ν and Y_ν are the Bessel functions of the first and second kind, respectively, of order ν, and $G^{m,n}_{p,q}\left(z|\mathbf{a}_p;\mathbf{b}_q\right)$ the Meijer G-function (Olver et al., 2010).

References

Alaminos-Quesada, J., Fernandez-Feria, R., 2020. Propulsion of a foil undergoing a flapping undulatory motion from the impulse theory in the linear potential limit. J. Fluid Mech. 883, 1–24, A19.

Alben, S., 2008. Optimal flexibility of a flapping appendage in an inviscid fluid. J. Fluid Mech. 614, 355–380.

Alben, S., Witt, C., Baker, T.V., Anderson, E., Lauder, G.V., 2012. Dynamics of freely swimming flexible foils. Phys. Fluids 24, 051901.

Anevlavi, D.E., Filippas, E.S., Karperaki, A.E., Belibassakis, K.A., 2020. A non-linear BEM-FEM coupled scheme for the performance of flexible flapping-foil thrusters. J. Mar. Sci. Eng. 8, 56.

Cleaver, D.J., Gursul, I., Calderon, D.E., Wang, Z., 2014. Thrust enhancement due to flexible trailing-edge of plunging foils. J. Fluids Struct. 51, 401–412.

Dagenais, P., Aegerter, C.M., 2020. How shape and flapping rate affect the distribution of fluid forces on flexible hydrofoils. J. Fluid Mech. 901, A1.

Demirer, E., Wang, Y.-C., Erturk, A., Alexeev, A., 2021. Effect of actuation method on hydrodynamics of elastic plates oscillating at resonance. J. Fluid Mech. 910, A4.

Dewey, P.A., Boschitsch, B.M., Moored, K.W., Stone, H.A., Smits, A.J., 2013. Scaling laws for the thrust production of flexible pitching panels. J. Fluid Mech. 732, 29–46.

Fernandez-Feria, R., 2016. Linearized propulsion theory of flapping airfoils revisited. Phys. Rev. Fluids 1, 084502.

Fernandez-Feria, R., 2017. Note on optimum propulsion of heaving and pitching airfoils from linear potential theory. J. Fluid Mech. 826, 781–796.

Fernandez-Feria, R., Alaminos-Quesada, J., 2021a. Analytical results for the propulsion performance of a flexible foil with prescribed pitching and heaving motions and passive small deflection. J. Fluid Mech. 910, A43.

Fernandez-Feria, R., Alaminos-Quesada, J., 2021b. Propulsion and energy harvesting performances of a flexible thin airfoil undergoing forced heaving motion with passive pitching and deformation of small amplitude. J. Fluids Struct. 102, 103255.

Floryan, D., Rowley, C.W., 2018. Clarifying the relationship between efficiency and resonance for flexible inertial swimmers. J. Fluid Mech. 853, 271–300.

Garrick, I.E., 1936. Propulsion of a Flapping and Oscillating Airfoil. Tech. Rep. TR 567, NACA.

Goza, A., Floryan, D., Rowley, C., 2020. Connections between resonance and nonlinearity in swimming performance of a flexible heaving plate. J. Fluid Mech. 888, A30.

Heathcote, S., Gursul, I., 2007. Flexible flapping airfoil propulsion at low Reynolds numbers. AIAA J. 45, 1066–1079.

Katz, J., Weihs, D., 1978. Hydrodynamic propulsion by large amplitude oscillation of an aerofoil with chordwise flexibility. J. Fluid Mech. 88, 485–497.

Long, R.L., 1961. Mechanics of solids and fluids. Prentice-Hall, Englewood Cliffs.

Mackowski, A.W., Williamson, C.H.K., 2017. Effect of pivot point location and passive heave on propulsion from a pitching airfoil. Phys. Rev. Fluids 2, 013101.

Manjunathan, S.A., Bhardwaj, R., 2020. Thrust generation by pitching and heaving of an elastic plate at low reynolds number. Phys. Fluids 32, 073601.

Michelin, S., Llewellyn Smith, S.G., 2009. An unsteady point vortex method for coupled fluid-solid problems. Theor. Comput. Fluid Dyn. 23, 127–153.

Moore, M.N.J., 2014. Analytical results on the role of flexibility in flapping propulsion. J. Fluid Mech. 757, 599–612.

Moore, M.N.J., 2015. Torsional spring is the optimal flexibility arrangement for thrust production of a flapping wing. Phys. Fluids 27, 091701.

Moore, M.N.J., 2017. A fast Chebyshev method for simulating flexible-wing propulsion. J. Comput. Phys. 345, 792–817.

Newmark, N.M., 1959. A method of computation for structural dynamics. J. Eng. Mech. ASCE 85, 67–94.

Olivier, M., Dumas, G., 2016. A parametric investigation of the propulsion of 2D chordwise-flexible flapping wings at low Reynolds number using numerical simulations. J. Fluids Struct. 63, 210–237.

Olver, F.W.J., Lozier, D.W., Boisvert, R.F., Clark, C.W. (Eds.), 2010. NIST Handbook of Mathematical Functions. Cambridge University Press, Cambridge, UK.

Paraz, F., Schouvelier, L., Eloy, C., 2016. Thrust generation by a heaving foil: Resonance, nonlinearities, and optimality. Phys. Fluids 28, 011903.

Quinn, D.B., Lauder, G.V., Smits, A.J., 2014. Scaling the propulsive performance of heaving flexible panels. J. Fluid Mech. 738, 250–267.

Ramananarivo, S., Godoy-Diana, R., Thiria, B., 2011. Rather than resonance, flapping wings flyers may play on aerodynamics to improve performance. Proc. Natl. Acad. Sci. USA 108, 5964–5969.

Shin, S., Bae, S.Y., Kim, I.C., Kim, Y.J., 2009. Effects of flexibility on propulsive force acting on a heaving foil. Ocean Eng. 36, 285–294.

Theodorsen, T., 1935. General Theory of Aerodynamic Instability and the Mechanism of Flutter. Tech. Rep. TR 496, NACA.

Tzezana, G.A., Breuer, K.S., 2019. Thrust, drag and wake structure in flapping compliant membrane wings. J. Fluid Mech. 862, 871–888.

Wang, W., Huang, H., Lu, X.-Y., 2020. Optimal chordwise stiffness distribution for self-propelled heaving flexible plates. Phys. Fluids 32, 11905.

Wu, X., Zhang, X., Tian, X., Li, X., Lu, W., 2020. A review on fluid dynamics of flapping foils. Ocean Eng. 195, 106712.

Zhu, Q., 2007. Numerical simulation of a flapping foil with chodwise or spanwise flexibility. AIAA J. 45, 2448–2457.